## Original Article
# Assessment of an elastin binding molecule for PET imaging of atherosclerotic plaques

Cindy R Fischer[1], Adrienne Müller[1], Bianca Bochsler[1], Zoran Rancic[2], Philipp Kaufmann[3], Roger Schibli[1,4], Simon M Ametamey[1]

[1]Center for Radiopharmaceutical Sciences of ETH, PSI and USZ, Department of Chemistry and Applied Biosciences of ETH Zurich, Wolfgang-Pauli Strasse 10, CH-8093 Zurich, Switzerland; [2]Clinic for Cardiovascular Surgery, University Hospital Zurich, Rämistrasse 100, CH-8091 Zurich, Switzerland; [3]Cardiac Imaging, University Hospital Zurich, Rämistrasse 100, CH-8091 Zurich, Switzerland; [4]Center for Radiopharmaceutical Sciences of ETH, PSI and USZ, Paul Scherrer Institute, Department Biology and Chemistry, CH-5232 Villigen-PSI, Switzerland

**Abstract:** Elastin is considered as a key player in human vascular diseases and it might contribute to the development of atherosclerosis. The elastin binding radiotracer, [$^{18}$F]AlF-NOTA-EBM ([$^{18}$F]2), was evaluated in a wild type mouse to determine its *in vivo* distribution and on human carotid atherosclerotic plaque tissues to assess its utility as a PET imaging agent for visualizing human atherosclerotic plaque lesions. The free ligand NOTA-EBM, which served as the precursor, was obtained in 25% chemical yield. The radiosynthesis of [$^{18}$F]2 was accomplished by coordination of Al$^{18}$F to NOTA-EBM in 8-13% decay corrected radiochemical yield ($n$ = 7) and specific radioactivity of 59 ± 12 GBq/μmol. A dynamic *in vivo* PET scan in a healthy wild type mouse (C57BL/6) showed high accumulation of radioactivity in heart and lungs, organs reported to have high elastin content. Excretion of [$^{18}$F]2 proceeded via the renal pathway and through the hepatobiliary system as indicated by a high uptake of radioactivity in the liver, intestines and gall bladder. *In vitro* autoradiography on human atherosclerotic plaque sections showed a heterogeneous distribution of [$^{18}$F]2 with an elevated accumulation in stable and vulnerable atherosclerotic plaques compared to control samples of normal arteries. However, there was no statistical significance between the different plaque phenotypes and control samples. Competition experiments with 10.000-fold excess of free ligand NOTA-EBM resulted in a marked decrease of radioactivity accumulation, consistent with a target-specific ligand.

**Keywords:** Elastin, atherosclerotic plaques, PET imaging, autoradiography, Al$^{18}$F

## Introduction

Cardiovascular disease (CD) is currently the most frequent cause of death and illness in industrial countries and the prognosis of the World Health Organization (WHO) is that CD will soon become the leading health problem worldwide [1]. Atherosclerosis, an inflammatory disease characterized by the accumulation of lipids and fibrous elements in the intima of the artery walls, plays a key role in the pathogenesis of cardiovascular diseases. Myocardial infarction or stroke can result from expansion and destabilization of atherosclerotic lesions, leading to plaque rupture and subsequent thrombotic events [2-5]. Prevention of serious cardiovascular events has therefore been linked to early diagnosis and detection of atherosclerotic lesions. In the last years, much

effort has been put on various non-invasive imaging techniques to detect the presence of plaque lesions. Imaging modalities such as ultrasound, computed tomography (CT), magnetic resonance imaging (MRI) and nuclear imaging methods like single photon computed tomography (SPECT) and positron emission tomography (PET) provide information with diagnostic and prognostic value but each imaging approach presents advantages and weaknesses [6-11]. A foremost advantage of nuclear imaging is the excellent sensitivity and administration of only low mass doses resulting in picomolar levels at the target site compared with MRI and CT, where higher mass doses ($10^{-3}$ - $10^{-5}$ M) of contrast agent are used [12, 13].

The extracellular matrix (ECM) plays a critical role during the development of atherosclerosis

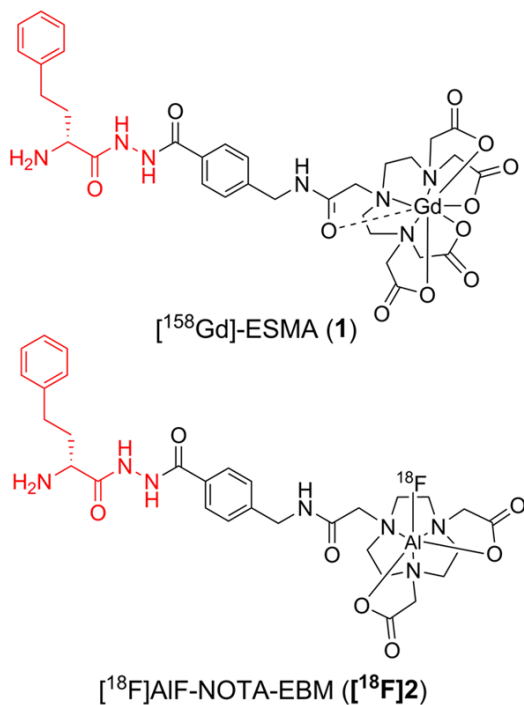$[^{158}Gd]$-ESMA (**1**)

$[^{18}F]AlF$-NOTA-EBM ($[^{18}F]$**2**)

**Figure 1.** Chemical structures of the gadolinium-containing elastin-specific MRI contrast agent $[^{158}Gd]$-ESMA (**1**) and the novel $Al^{18}F$-labeled NOTA-coupled elastin binding molecule $[^{18}F]AlF$-NOTA-EBM ($[^{18}F]$**2**). The elastin binding part is highlighted in red.

providing the structural integrity of the plaques and participating in several key events to regulate cell function [14, 15]. Degradation of the ECM can lead to plaque instability and subsequent plaque rupture, whereas enhanced synthesis of the ECM leads to vessel wall remodelling and contributes to plaque stabilization [14]. The structural protein elastin is the dominant extracellular matrix protein deposited in the arterial wall and can contribute up to 50% of its dry weight [16]. Elastin is the main component of elastic fibers, which provides elasticity and resilience to many tissues such as skin, lungs, ligaments and arterial walls [15, 17]. It is known that smooth muscle cells are the elastin-producing cells in plaques [14, 15, 18]. As an additional source for this matrix protein, Krettek *et al.* identified human macrophages within plaques producing the elastin precursor tropoelastin [19]. Therefore, elastin is considered as a key player in human vascular diseases and it might contribute to the development of atherosclerosis [20].

A recent study published by Makowski and co-workers showed that atherosclerotic plaque

burden in an ApoE^{-/-} mouse model could be imaged with an elastin-specific MRI contrast agent ESMA (**1**, **Figure 1**) [21]. Quantitative changes of the plaque matrix elastin content at various stages of atherosclerosis in comparison to healthy arteries were visualized through signal intensity measurements. *In vivo* competition experiments with non-paramagnetic ESMA resulted in a marked decrease of the signal, consistent with a target-specific contrast agent. Electron microscopy studies also showed a marked co-localization of ESMA with elastic fibers [21].

These encouraging results prompted us to investigate whether an ESMA-based PET radioligand can be used to image atherosclerotic plaques. Consequently, we modified ESMA with a macrocyclic chelator, 1,4,7-triazacyclononane-1,4,7-triacetic acid (NOTA), such that the resulting elastin binding molecule (EBM) is amenable to radiolabeling with a positron emitting radionuclide. NOTA is a suitable chelator that is known to form stable complexes with various radionuclides such as $^{68}Ga$, $^{64}Cu$ and $Al^{18}F$ [22, 23].

In this work, we report a proof of concept study with the $Al^{18}F$-labeled NOTA-coupled elastin binding molecule, $[^{18}F]AlF$-NOTA-EBM ($[^{18}F]$**2**, **Figure 1**).

This novel radiotracer was evaluated in a wild type mouse (C57BL/6) to determine its *in vivo* distribution and *in vitro* on human carotid atherosclerotic plaque sections to assess its potential for imaging atherosclerotic plaque lesions.

**Material and methods**

*General*

Reagents and solvents were purchased from Sigma-Aldrich, Merck AG, VWR International AG or Bachem. All chemicals were used as supplied unless stated otherwise. Low resolution mass spectra (LRMS) were recorded with a Micromass Quattro micro API LC-ESI and high resolution mass spectra (HRMS) with a Bruker FTMS 4.7 T BioAPEXII spectrometer (ESI). Nuclear magnetic resonance spectra were recorded on a Bruker 400 MHz spectrometer with the corresponding solvent signals as an internal standard. Chemical shifts are reported
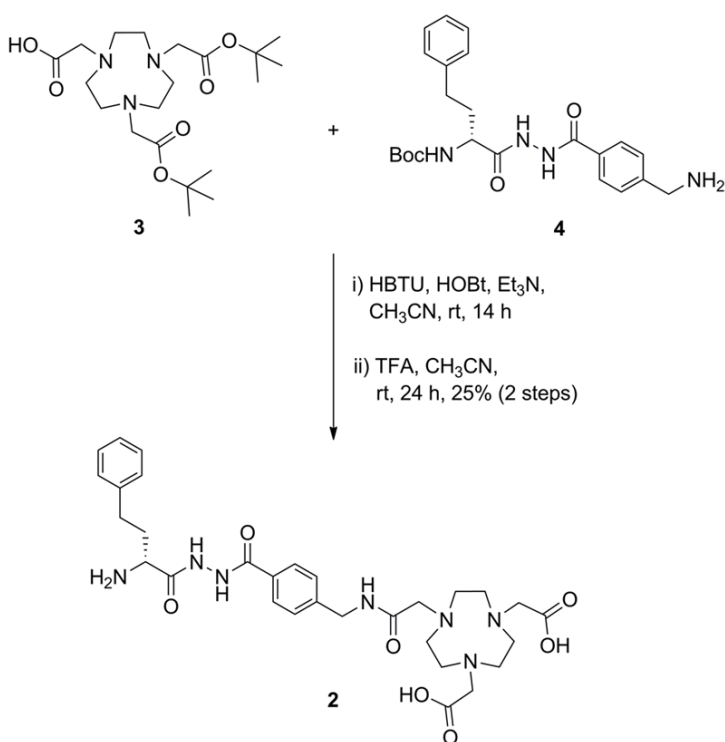
**Figure 2.** Synthesis of the free ligand **2** from key intermediate **4** *via* coupling reaction with protected NOTA derivative **3**.

in parts per million (ppm) relative to tetramethylsilane (0.00 ppm). Values of the coupling constant, *J*, are given in hertz (Hz); the following abbreviations are used in the experimental section for the description of $^1$H-NMR spectra: singlet (s), doublet (d), triplet (t) and multiplet (m). Reactions were monitored by thin layer chromatography (TLC, performed on Merck precoated silica gel 60 F-254 aluminium plates) or high performance liquid chromatography (HPLC). HPLC was performed on a Merck-Hitachi L7000 system equipped with a L7400 tunable absorption detector. Analytical HPLC was performed with a reversed-phase column (Gemini-NX C18, 5 *µm*, 4.6 × 250 mm, Phenomenex) using 0.1% TFA in water (solvent A) and acetonitrile (solvent B) as a solvent system with a gradient from 0 - 12 min 85% A, 12 - 17 min 85 - 30% A, 17 - 25 min 30% A and a flow rate of 1 mL/min. Preparative HPLC was performed with a reversed-phase preparative column (Ultisil™ former Ultimate C18, 5 *µm*, 21.2 × 150 mm, Welch Materials) at a flow rate of 18 mL/min with 0.1% TFA in water (solvent A) and acetonitrile (solvent B) as solvent system and a gradient as follows: 0 - 20 min 100 - 70% A, 20 - 28

min 70 - 30% A, 28 - 34 min 30% A. Analytical radio-HPLC was performed on a Merck-Hitachi L2130 system equipped with a L2450 diode array detector and a Berthold radiodetector with a reversed-phase column (Gemini C18-NX, 5 *µm*, 4.6 × 250 mm, Phenomenex) using 0.1% TFA in water (solvent A) and acetonitrile (solvent B) as solvent system with a gradient from 0 - 16 min 85% A, 16 - 22 min 85 - 30% A, 22 - 30 min 30% A and a flow rate of 1 mL/min. Semi-preparative radio-HPLC was performed on a HPLC system equipped with a Merck-Hitachi L6200A intelligent pump, a Knauer variable-wavelength ultraviolet detector and an Eberline RM14 radiodetector. [$^{18}$F]**2** was purified on a reversed-phase semi-preparative column (Gemini C18, 5 µm, 250 x 10 mm, Phenomenex) at a flow rate of 4 mL/min with 0.1% TFA in water (solvent A) and acetonitrile (solvent B) as solvent system and a gradient as follows: 0 - 3 min 100% A, 3 - 4 min 100 - 85% A, 4 - 20 min 85% A, 20 - 26 min 85 - 30% A, 26 - 40 min 30% A.

Specific radioactivity was determined by analytical radio-HPLC from a calibration curve obtained from different concentrations of the free ligand **2**.

*Synthesis of free ligand NOTA-EBM (2)*

The synthesis of the free ligand **2** from key intermediate **4** *via* coupling reaction with NOTA derivative **3** is illustrated in **Figure 2**. Key intermediate **4** was prepared according to a published patent [24] in analogy to the elastin-specific MRI contrast agent ESMA (BMS753951) reported by Makowski *et al*. [21].

To a solution of NOTA(tBu)$_2$ (**3**, 199.5 mg, 0.48 mmol) in acetonitrile (10 mL) HBTU (182.6 mg, 0.48 mmol), HOBt (65.4 mg, 0.48 mmol) and Et$_3$N (0.27 mL, 1.92 mmol) were added. Compound **4** (245.8 mg, 0.58 mmol) was dissolved in acetonitrile (2 mL) and added to the reaction mixture in one portion. Thereafter, the solution was stirred at ambient temperature for

14 h and then concentrated *in vacuo*. The residue was dissolved in ethylacetate (50 mL) and washed with 10% aqueous citric acid (3 × 25 mL), sat. aqueous $NaHCO_3$-solution (3 × 25 mL) and brine (25 mL). After drying over $Na_2SO_4$, the solution was concentrated under reduced pressure and the protected NOTA derivative was used for the next step without further purification. LR-MS (ES$^+$) calculated for $C_{43}H_{65}N_7O_9$: 825.02; found: 825.67.

For deprotection, the protected NOTA derivative was dissolved in acetonitrile (5 mL) and TFA (5 mL) and stirred 24 h at ambient temperature. The reaction progress was monitored by HPLC. For isolation of the product, the mixture was submitted to preparative HPLC. The desired fraction was collected and lyophilized to provided product **2** as a white powder (73 mg, 25% over two steps, purity according to HPLC > 86%).

$^1$H-NMR (DMSO-d6) δ/ppm 2.14 (m, 2H), 2.82 (m, 2H), 3.05 (m, 12H), 3.68 (s, 4H), 3.85 (s, 2H), 4.07 (m, 1H), 4.44 (d, J = 5.9 Hz, 2H), 7.28 (m, 2H), 7.37 (t, J = 7.5 Hz, 2H), 7.48 (m, 3H), 7.92 (m, 2H), 8.47 (s, 2H), 8.81 (t, J = 5.9 Hz, 1H), 10.61 (d, J = 12.8 Hz, 2H); HRMS (ES$^+$) calculated for $C_{30}H_{42}N_7O_7$: 612.3140; found: 612.3139.

*Radiochemistry*

No-carrier-added [$^{18}$F]fluoride was produced via the $^{18}$O(p,n)$^{18}$F nuclear reaction at a Cyclone 18/9 cyclotron (IBA, Belgium) by irradiation of enriched $^{18}$O-water. [$^{18}$F]fluoride was immobilized on an anion-exchange cartridge (QMA Light; Waters; preconditioned with 0.5 M $CH_3COONa$-solution (5 mL, pH 8.8) and $H_2O$ (5 - 10 mL)) and eluted with 0.9% NaCl-solution. [$^{18}$F]fluoride (ca. 15 GBq) in ca. 50 µL saline was mixed with 80 µL free ligand solution **2** (2 mM, 160 nmol) in 0.1 M NaOAc (pH 4) and 40 µL $AlCl_3$ solution (2 mM, 80 nmol) in 0.1 M NaOAc (pH 4) in a 5 mL sealed reaction vessel. The reaction mixture was incubated at 105°C for 15 min. After cooling for 5 min, 4 mL of water was added to the reactive vial and the mixture was purified by semi-preparative radio-HPLC. The product fraction was collected into 20 mL of water and the mixture was passed through a reversed-phase cartridge (Sep-Pak C18 light; Waters; preconditioned with EtOH (5 mL) and $H_2O$ (5 mL)) to remove acetonitrile. The cartridge was washed with 10 mL of water and

the $^{18}$F-labeled product [$^{18}$F]**2** was eluted with 0.5 mL of ethanol into a sterile, pyrogen-free vial and diluted with 5 mL water for stability studies. Samples of [$^{18}$F]**2** were taken at different time points and analyzed by analytical radio-HPLC. For PET imaging studies, the solution of [$^{18}$F]**2** in water was diluted with 4.5 mL of 0.9% NaCl-solution, whereas for *in vitro* autoradiography studies, [$^{18}$F]**2** was diluted with TRIS buffer (50 mM Tris, 150 mM NaCl, pH 7.4) to a final radiotracer concentration of 50 nM.

*Determination of distribution coefficient*

The distribution coefficient (logD$_{7.4}$) was determined by the shake flask method. In brief, [$^{18}$F]**2** was dissolved in a mixture of phosphate buffer (500 µL, pH 7.4) and *n*-octanol (500 µL) at 20°C. Thereafter, the sample was equilibrated for 15 min in an over-head shaker and the two phases were separated by centrifugation (3 min, 5000 rpm). Aliquots (50 µL) of both phases were analyzed in a γ-counter (Wizard, PerkinElmer). The partition coefficient was expressed as the ratio between the radioactivity concentrations (cpm/mL) of the *n*-octanol and the buffer phase. Values represent the mean ± standard deviation of eight determinations from two independent experiments.

*In vivo PET imaging studies*

Five-week-old male C57BL/6 mice were obtained from Charles River (Germany). Animal care and all experimental procedures were approved by Cantonal Veterinary Office in Zurich, Switzerland. Animals had free excess to food and water. PET experiments were performed with an eXplore VISTA PET/CT tomograph (Sedecal, Spain/GE Healthcare) with a maximum resolution of 2 mm full width at half maximum [25]. Anesthesia was induced with isoflurane in an air/oxygen mixture and one animal was injected with 13 MBq (4.2 nmol) of [$^{18}$F]**2** *via* a lateral tail vein. A dynamic PET scan was acquired from 0 - 90 min post injection (p.i.). After acquisition, PET data were reconstructed in user-defined time frames and fused datasets of PET and CT were analyzed with PMOD software (version 3.4).

*Human carotid atherosclerotic tissue bank*

This study was conducted with excised tissue from 25 patients referred to the clinic for car-

**Table 1.** Characteristics of the patients included in this study

| Characteristics | |
|---|---|
| Patients | 25 |
| Female/Men | 2/23 |
| Age at surgery (y) | 72 ± 7 |
| Normal arteries | 7 |
| Stable plaques | 13 |
| Vulnerable plaques | 10 |

Data are mean ± SD or *n*.

diovascular surgery of the University Hospital of Zurich for carotid endarterectomy (CEA). Written informed consent was obtained from all patients. The atherosclerotic plaques were removed from the internal, common or external carotid artery as previously described [26]. After dissection, the tissues were immediately frozen and stored at 80°C until sectioned. According to the classification of the American Heart Association, plaques were characterized as stable if they macroscopically presented a lipid core encapsulated between a fibrous cap and the media without endothelial disruption. Plaques were considered vulnerable if there was intraplaque hemorrhage evolving in the necrotic core, disruption of the surface or thrombosis [27, 28]. These macroscopic features of vulnerable plaques or the presence of the intact fibrous cap in stable plaques were confirmed by histological analysis such as hematoxylin and eosin and Masson Goldner's trichrom staining (data not shown). The microscopic classification was in agreement with the macroscopic classification. Furthermore, for division into vulnerable plaques, the threshold of the representative cap thickness was considered to be < 500 µm and of the minimum cap thickness < 200 µm in carotid plaques [29]. In this study, human tissue samples of vulnerable plaques, stable plaques and samples of normal artery walls as controls were used. **Table 1** summarizes the characteristics of the patients in this study.

Hearts from 6-week-old Wistar rats (Charles River, Germany) were used as positive control and internal standard.

*In vitro autoradiography studies*

Frozen transversal slices (20 µm) adsorbed to SuperFrost Plus slides were thawed at ambient temperature and preincubated on ice for 15 min in TRIS buffer (50 mM Tris, 150 mM NaCl, pH 7.4 at 4°C) containing 0.1% bovine serum albumin (BSA). Excess solution was carefully removed, and slides were incubated with 50 nM [$^{18}$F]2 alone or together with 500 µM **2** in TRIS buffer for 45 min at ambient temperature. After incubation, the solutions were decanted and the slides washed in TRIS buffer containing 0.1% BSA (5 min), three times in TRIS buffer (5 min each) and finally dipped twice in distilled water, all steps at 4°C. To generate a calibration curve, a dilution series of the radiotracer [$^{18}$F]2 was prepared and pipetted on filter papers. Dried slides and filter papers were exposed to the same phosphor imager plate (BAS-MS 2025, Fuji) for 15 min, and the plate was scanned in a BAS5000 reader (Fuji). Quantitative examination was performed with the AIDA evaluation software. The maximum intensity of each tissue section was determined, the background was subtracted and the amount of radiotracer bound to the tissue was calculated using the calibration curve. All patient samples were normalized to values from the rat heart whereby the maximal bound radiotracer was set to 1. Afterwards, the sections were stained by hematoxylin and eosin.

*Statistical analysis*

Statistical analyses were performed by using the unpaired two-tailed Student's *t*-test (*Graph Pad Prism* 6.0 software). A *P*-value of ≤ 0.05 was considered statistically significant.

**Results**

*Chemistry and radiochemistry*

The synthesis of key intermediate **4** was accomplished in 49% chemical yield according to the procedure published by Harris *et al.* [24]. Intermediate **4** was coupled to commercially available NOTA derivative **3** using HBTU as a coupling reagent [30] (**Figure 2**). The protected NOTA-EBM derivative was used for the next step without further purification. After deprotection of the Boc-group with TFA and purification by HPLC, precursor compound **2** was obtained as a white solid in 25% chemical yield. The radiosynthesis of [$^{18}$F]2 was performed in analogy to a previously published procedure [31, 32]. [$^{18}$F]2 was accomplished by coordination of Al$^{18}$F under slightly acidic conditions in 20 - 25% incorporation yield. After HPLC-
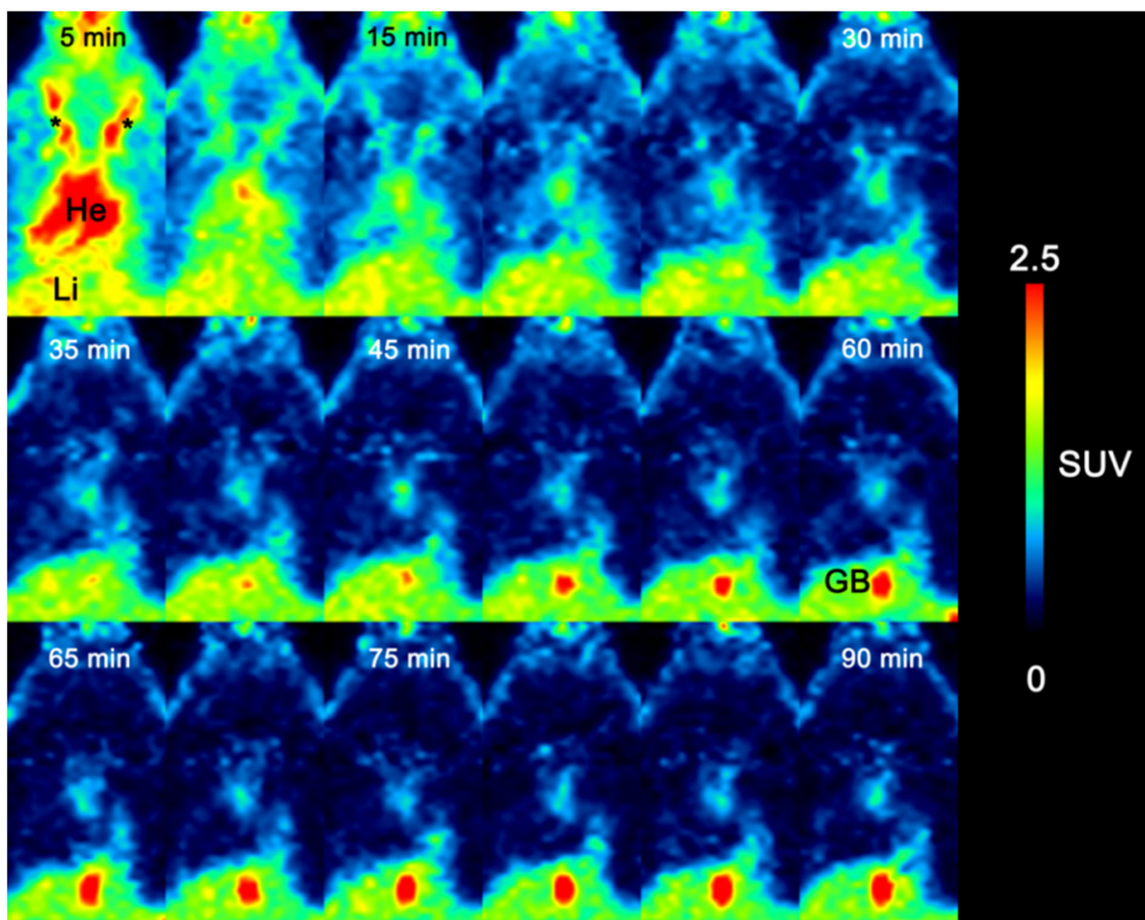
**Figure 3.** PET images showing coronal sections of a wild type mouse from 0 to 90 min acquisition after injection of 13 MBq (4.2 nmol) of [$^{18}$F]2. Each section represents a 5 min time frame (He: heart with *carotid arteries in the neck region, Li: liver, GB: gall bladder).

purification, the target compound was obtained in a decay-corrected radiochemical yield of 8 - 13% (n = 7). Typically, starting from 10 - 15 GBq of [$^{18}$F]-fluoride, 0.5 - 1.4 GBq of isolated product were obtained after an overall synthesis time of ~1 h. The radiochemical purity of [$^{18}$F]2 was $\geq$ 95%, with a specific radioactivity (EOS) of 59 $\pm$ 12 GBq/µmol. The logD$_{7.4}$ value of [$^{18}$F]2 was -1.3 $\pm$ 0.1 and stability studies of [$^{18}$F]2 revealed no defluorination or radioactive degradation products within 120 min at room temperature, which was confirmed by analytical radio-HPLC.

*In vivo PET imaging*

A dynamic PET scan was performed with a wild type mouse to determine the *in vivo* distribution of [$^{18}$F]2. **Figure 3** shows a time series of coronal sections from the heart and neck

region after [$^{18}$F]2 application. Each section represents a 5 min time frame.

In early time frames up to 15 min p.i., high accumulation of radioactivity was found in the carotid arteries and heart region. After approximately 15 min p.i. the accumulation of radioactivity in the carotid arteries decreased, whereas uptake of [$^{18}$F]2 remained high in heart and liver. Starting from 40 min p.i. a high accumulation of radioactivity was observed in the gall bladder.

In **Figure 4** different coronal sections of [$^{18}$F]2 uptake averaged from 0 to 90 min p.i. are shown. High uptake of radioactivity was observed in the lungs and the heart, organs known to have high elastin content. Accumulation of [$^{18}$F]2 was also visible in the animal skin and paws. Excretion organs such
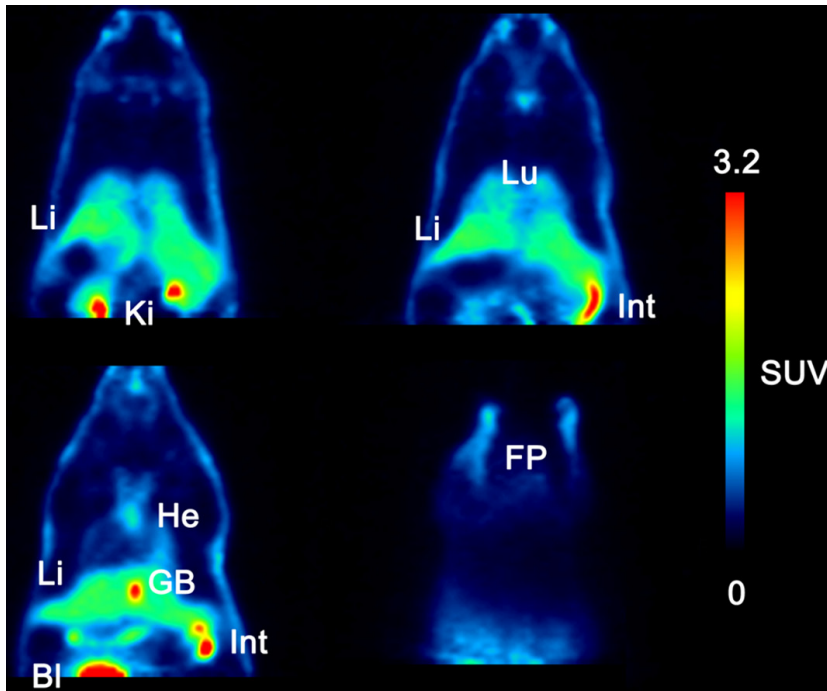
**Figure 4.** Different coronal slices of a PET image of a wild type mouse averaged from 0 to 90 min after injection of 13 MBq (4.2 nmol) of [$^{18}$F]2 (Li: liver, Ki: kidneys, Lu: lungs, Int: intestines/feces, He: heart, GB: gall bladder, FP: front paws).

were used for *in vitro* autoradiography studies. A rat heart served as a positive control and as an internal standard for later quantifications. All human tissue samples showed a heterogeneous accumulation of [$^{18}$F]2. Rat hearts showed generally higher binding of the radiotracer than the patient samples (**Figure 5**). Several hot spots of radioactivity were observed in atherosclerotic plaque samples. With an 10.000-fold excess of the free ligand **2**, accumulation of [$^{18}$F]2 decreased in all tissue samples.

In **Figure 6** are depicted the normalized accumulation values of the human tissue samples grouped according to their phenotype. There was a trend towards a higher accumulation of [$^{18}$F]2 in stable and vulnerable atherosclerotic plaques but no statistical significance could be detected between samples of normal arteries and atherosclerotic plaques (normal arteries vs. stable plaques: $P = 0.44$; normal arteries vs. vulnerable plaques: $P = 0.15$) as well as between both plaque phenotypes ($P = 0.55$).
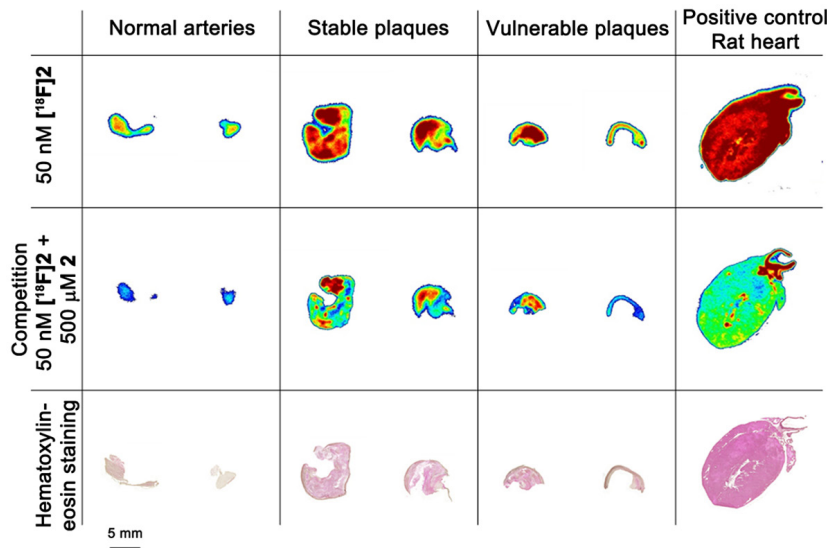


**Figure 5.** Representative examples of human atherosclerotic plaque and rat heart sections incubated with [$^{18}$F]2 alone (first row) or with excess of the free ligand **2** (middle row). The bottom row shows hematoxylin-eosin staining of the samples.

as kidneys, liver, intestines and gall bladder showed a high uptake of radioactivity.

*In vitro autoradiography studies*

Human carotid artery vessels with different plaque phenotypes or from normal arteries

**Discussion**

Imaging techniques currently being used in the clinic to identify atherosclerotic plaques include ultrasound, CT, MRI and nuclear imaging methods like SPECT and PET. Early detection of the
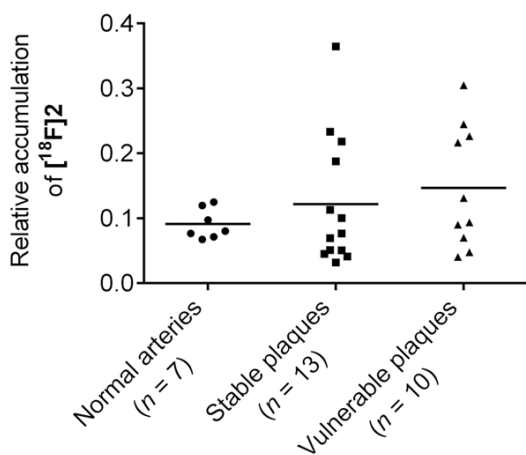
**Figure 6.** Normalized data of [¹⁸F]2 accumulation in tissue sections obtained by *in vitro* autoradiography (rat heart as internal standard is set to 1). Atherosclerotic samples were grouped according to their phenotype. The lines represent the mean of each group.

life-threatening vulnerable atherosclerotic plaques using one of these imaging modalities would be an important step towards patient care and management. So far, 2-deoxy-2-[¹⁸F] fluoro-D-glucose [¹⁸F]FDG is the most commonly used radiotracer in the clinic for the PET imaging of atherosclerosis but is limited by its lack of cellular specificity [10]. As such, more specific radiotracers are needed.

In a recent study, Makowski and co-workers followed the progression and regression of plaque burden in an ApoE⁻/⁻ mouse model using the elastin-specific MRI contrast agent ESMA. Changes in the content of elastin in atherosclerotic plaques in comparison to healthy arteries were demonstrated [21].

Our goal was to verify whether ESMA radiolabeled with an appropriate PET radionuclide can be used to visualize plaque burden. To this end, we designed and prepared [¹⁸F]AIF-NOTA-EBM as a potential elastin binding PET radiotracer. Complexation reactions of Al¹⁸F with NOTA have recently being reported by a number of research groups [23, 31-36]. The reactions are generally efficient and afford stable compounds in optimal radiochemical yields. We find it attractive to use this technique for the ¹⁸F-labeling of NOTA-EBM.

The synthesis of the precursor compound **2** was achieved in a two-step procedure (**Figure**

**2**). The coupling of the NOTA chelator to compound **4**, which was synthesized in good yields in analogy to a published procedure by Harris *et al.* [24], was accomplished using HBTU as a coupling reagent. After a deprotection step, compound **2** was obtained in 25% chemical yield. NMR spectroscopy and high resolution mass spectrometry confirmed the structure of NOTA-EBM.

The radiosynthesis of [¹⁸F]2 was achieved in a decay corrected radiochemical yield of 8-13% ($n = 7$) and a specific radioactivity (EOS) of $59 \pm 12$ GBq/μmol. Due to the formation of radiolabeled by-products, purification by semi-preparative HPLC was necessary. Purification using cartridges was not possible due to the similar elution profile of [¹⁸F]2 and side-products. An explanation for the occurrence of by-products could be the moderate purity (> 86%) of the precursor, NOTA-EBM.

In order to determine the *in vivo* behaviour and distribution of [¹⁸F]2, an *in vivo* PET scan in a wild type mouse was performed. This PET study showed that [¹⁸F]2 is excreted not only through the kidneys but also through the hepatobiliary system as indicated by a high uptake of [¹⁸F]2 in the liver, intestines and gall bladder. The determined $logD_{7.4}$ value of $-1.3 \pm 0.1$ for [¹⁸F]2 suggested that the radiotracer is relatively hydrophilic and that its clearance may predominately proceed *via* the renal excretion pathway. [¹⁸F]2 was slowly cleared from the blood pool within the first 30 min after injection. For the imaging of carotid plaques, this would suggest later time points in order to achieve better target-to-background ratios. In general, a high uptake of the radiotracer [¹⁸F]2 was observed in organs such as lungs and heart, reported to have prominent elastin content [15, 17]. Similar high accumulation of [¹⁸F]2 was also observed to the animal skin and paws in the PET image corroborating literature data that paws and skin of rodents are also rich in elastic fibers, which are made of the structural protein elastin [17, 37].

Encouraged by the *in vivo* behavior of [¹⁸F]2, we performed *in vitro* autoradiography studies on human carotid plaque sections and found a heterogeneous accumulation of [¹⁸F]2 to phenotypically different plaque samples. Compared to all plaque samples, the rat heart showed the highest binding of [¹⁸F]2. Due to the known high

and evenly distribution of elastin in the rodent heart [15, 17], the rat heart served as an internal standard in this study.

Competition experiments with 10.000-fold excess of free ligand **2** resulted in a marked decrease of radioactivity accumulation, suggesting competition for the same binding sites. Compared to human control samples of normal arteries, a higher binding of [18F]**2** was observed in stable and vulnerable atherosclerotic plaques, however, no clear differentiation between stable and vulnerable atherosclerotic plaques was evident. The higher uptake of [18F]**2** in stable and vulnerable atherosclerotic plaques may be explained by the increased extracellular matrix remodelling in atherosclerotic plaque progression and smooth muscle cell proliferation [14, 15, 18, 20].

### Conclusions

The radiosynthesis of [18F]AlF-NOTA-EBM was accomplished in optimal radiochemical yields and high specific radioactivity. The novel elastin binding radiotracer [18F]**2**, exhibited high binding to organs with high elastin content. *In vitro* autoradiography studies using human atherosclerotic plaque tissues from carotid vessels, revealed higher accumulation of [18F]**2** in plaque samples compared to control samples of normal arteries, however no statistical significance was evident. [18F]AlF-NOTA-EBM might thus not be a useful imaging agent for visualizing atherosclerotic plaques in carotid arteries by PET.

### Acknowledgements

### Disclosure of conflict of interest

None.

**Address correspondence to:** Dr. Simon M Ametamey, Center for Radiopharmaceutical Sciences of ETH, PSI and USZ, Department of Chemistry and Applied Biosciences of ETH Zurich, Wolfgang-Pauli-Strasse 10, 8093 Zurich, Switzerland. Tel: +41 44 633 74 63; Fax: +41 44 633 13 67; E-mail: Simon. Ametamey@pharma.ethz.ch

### References

[1]   Lindholm LH and Mendis S. Prevention of cardiovascular disease in developing countries. Lancet 2007; 370: 720-722.

[2]   Lindsay AC and Choudhury RP. Form to function: current and future roles for atherosclerosis imaging in drug development. Nature Rev Drug Discovery 2008; 7: 517-529.

[3]   Sanz J and Fayad ZA. Imaging of atherosclerotic cardiovascular disease. Nature 2008; 451: 953-957.

[4]   Libby P, DiCarli M and Weissleder R. The vascular biology of atherosclerosis and imaging targets. J Nucl Med 2010; 51 Suppl 1: 33S-37S.

[5]   Libby P, Ridker PM and Hansson GK. Progress and challenges in translating the biology of atherosclerosis. Nature 2011; 473: 317-325.

[6]   Matter CM, Stuber M and Nahrendorf M. Imaging of the unstable plaque: how far have we got? Eur Heart J 2009; 30: 2566-2574.

[7]   Sadeghi MM, Glover DK, Lanza GM, Fayad ZA and Johnson LL. Imaging atherosclerosis and vulnerable plaque. J Nucl Med 2010; 51 Suppl 1: 51S-65S.

[8]   Vancraeynest D, Pasquet A, Roelants V, Gerber BL and Vanoverschelde JL. Imaging the vulnerable plaque. J Am Coll Cardiol 2011; 57: 1961-1979.

[9]   Owen DR, Lindsay AC, Choudhury RP and Fayad ZA. Imaging of atherosclerosis. Ann Rev Med 2011; 62: 25-40.

[10]  Joshi FR, Lindsay AC, Obaid DR, Falk E and Rudd JH. Non-invasive imaging of atherosclerosis. Eur Heart J Cardiovasc Imaging 2012; 13: 205-218.

[11]  Quillard T and Libby P. Molecular imaging of atherosclerosis for improving diagnostic and therapeutic development. Circulation Res 2012; 111: 231-244.

[12]  Ametamey SM, Honer M and Schubiger PA. Molecular imaging with PET. Chem Rev 2008; 108: 1501-1516.

[13]  Dobrucki LW and Sinusas AJ. PET and SPECT in cardiovascular molecular imaging. Nat Rev Cardiol 2010; 7: 38-47.

[14]  Katsuda S and Kaji T. Atherosclerosis and extracellular matrix. J Atheroscler Thromb 2003; 10: 267-274.

[15]  Wachi H. Role of elastic fibers on cardiovascular disease. J Health Sci 2011; 57: 449-457.

[16]  Karnik SK, Brooke BS, Bayes-Genis A, Sorensen L, Wythe JD, Schwartz RS, Keating MT

and Li DY. A critical role for elastin signaling in vascular morphogenesis and disease. Development 2003; 130: 411-423.

[17] Debelle L and Tamburro AM. Elastin: molecular description and function. Int J Biochem Cell Biol 1999; 31: 261-272.

[18] Long JL and Tranquillo RT. Elastic fiber production in cardiovascular tissue-equivalents. Matrix Biol 2003; 22: 339-350.

[19] Krettek A, Sukhova GK and Libby P. Elastogenesis in human arterial disease: a role for macrophages in disordered elastin synthesis. Arterioscler Thromb Vasc Biol 2003; 23: 582-587.

[20] Brooke BS, Bayes-Genis A and Li DY. New insights into elastin and vascular disease. Trends Cardiovasc Med 2003; 13: 176-181.

[21] Makowski MR, Wiethoff AJ, Blume U, Cuello F, Warley A, Jansen CH, Nagel E, Razavi R, Onthank DC, Cesati RR, Marber MS, Schaeffter T, Smith A, Robinson SP and Botnar RM. Assessment of atherosclerotic plaque burden with an elastin-specific magnetic resonance contrast agent. Nat Med 2011; 17: 383-8.

[22] Clarke ET and Martell AE. Stabilities of the Fe(III), Ga(III) and in(III) chelates of N,N',N''-triazacyclononanetriacetic acid. Inorg Chim Acta 1991; 181: 273-280.

[23] McBride WJ, Sharkey RM, Karacay H, D'Souza CA, Rossi EA, Laverman P, Chang CH, Boerman OC and Goldenberg DM. A novel method of $^{18}$F radiolabeling for PET. J Nucl Med 2009; 50: 991-998.

[24] Harris TD, Robinson SP, Cesati RR and Yalamanchili P. New hydrazide derivatives used for detecting, imaging and monitoring pathological disorder associated with e.g. coronary plaque, carotid plaque, aneurism and vasculitis. US Patent PCT/US2007014721-A1 2007.

[25] Wang Y, Seidel J, Tsui BM, Vaquero JJ and Pomper MG. Performance evaluation of the GE healthcare eXplore VISTA dual-ring small-animal PET scanner. J Nucl Med 2006; 47: 1891-1900.

[26] Nett PC, Zund G, Pretre R, Niederhouser U, Vogt PR and Turina M. A 20-year follow-up of internal carotid artery endarterectomy with bifurcation advancement. Thorac Cardiovasc Surg 2000; 48: 279-284.

[27] Stary HC, Chandler AB, Dinsmore RE, Fuster V, Glagov S, Insull W Jr, Rosenfeld ME, Schwartz CJ, Wagner WD and Wissler RW. A definition of advanced types of atherosclerotic lesions and a histological classification of atherosclerosis. A report from the Committee on Vascular Le-

sions of the Council on Arteriosclerosis, American Heart Association. Arterioscler Thromb Vasc Biol 1995; 15: 1512-1531.

[28] Pedretti M, Rancic Z, Soltermann A, Herzog BA, Schliemann C, Lachat M, Neri D and Kaufmann PA. Comparative immunohistochemical staining of atherosclerotic plaques using F16, F8 and L19: Three clinical-grade fully human antibodies. Atherosclerosis 2010; 208: 382-389.

[29] Redgrave JN, Gallagher P, Lovett JK and Rothwell PM. Critical cap thickness and rupture in symptomatic carotid plaques: the oxford plaque study. Stroke 2008; 39: 1722-1729.

[30] Tolmachev V, Altai M, Sandström M, Perols A, Karlström AE, Boschetti F and Orlova A. Evaluation of a maleimido derivative of NOTA for site-specific labeling of affibody molecules. Bioconjug Chem 2011; 22: 894-902.

[31] McBride WJ, D'Souza CA, Sharkey RM, Karacay H, Rossi EA, Chang CH and Goldenberg DM. Improved $^{18}$F labeling of peptides with a fluoride-aluminum-chelate complex. Bioconjug Chem 2010; 21: 1331-1340.

[32] McBride WJ, D'Souza CA, Sharkey RM and Goldenberg DM. The radiolabeling of proteins by the [$^{18}$F]AIF method. Appl Radiat Isot 2012; 70: 200-204.

[33] Laverman P, McBride WJ, Sharkey RM, Eek A, Joosten L, Oyen WJ, Goldenberg DM and Boerman OC. A novel facile method of labeling octreotide with $^{18}$F-fluorine. J Nucl Med 2010; 51: 454-461.

[34] D'Souza CA, McBride WJ, Sharkey RM, Todaro LJ and Goldenberg DM. High-yielding aqueous $^{18}$F-labeling of peptides via Al$^{18}$F chelation. Bioconjug Chem 2011; 22: 1793-1803.

[35] Liu S, Liu H, Jiang H, Xu Y, Zhang H and Cheng Z. One-step radiosynthesis of $^{18}$F-AIF-NOTA-RGD$_2$ for tumor angiogenesis PET imaging. Eur J Nucl Med Mol Imaging 2011; 38: 1732-1741.

[36] Guo N, Lang L, Li W, Kiesewetter DO, Gao H, Niu G, Xie Q and Chen X. Quantitative analysis and comparison study of [$^{18}$F]AIF-NOTA-PRGD2, [$^{18}$F]FPPRGD2 and [$^{68}$Ga]Ga-NOTA-PRGD2 using a reference tissue model. PLoS One 2012; 7: e37506.

[37] Wong J, Bennett W, Ferguson MW and McGrouther DA. Microscopic and histological examination of the mouse hindpaw digit and flexor tendon arrangement with 3D reconstruction. J Anat 2006; 209: 533-545.